

Article

Spaceborne GNSS-R from the SMAP Mission: First Assessment of Polarimetric Scatterometry over Land and Cryosphere

Hugo Carreno-Luengo *, Stephen Lowe, Cinzia Zuffada, Stephan Esterhuizen and Shadi Oveisgharan

NASA's Jet Propulsion Laboratory (JPL), California Institute of Technology, 4800 Oak Grove Drive, Pasadena, CA 91109, USA; stephen.lowe@jpl.nasa.gov (S.L.); cinzia.zuffada@jpl.nasa.gov (C.Z.);

Stephan.Esterhuizen@jpl.nasa.gov (S.E.); Shadi.Oveisgharan@jpl.nasa.gov (S.O.)

* Correspondence: hugo.carreno-luengo@jpl.nasa.gov; Tel.: +1-818-354-1924

Academic Editors: Nicolas Baghdadi and Prasad S. Thenkabail

Received: 21 December 2016; Accepted: 7 April 2017; Published: 12 April 2017

Abstract: This work describes the first global scale assessment of a Global Navigation Satellite Systems Reflectometry (GNSS-R) experiment performed on-board the Soil Moisture Active Passive (SMAP) mission for soil moisture and biomass determination. Scattered GPS L2 signals (1227.6 MHz) were collected by the SMAP's dual-polarization (Horizontal H and Vertical V) radar receiver and then processed on-ground using a known replica of the GPS L2C code. The scattering properties over land are evaluated using the Signal-to-Noise Ratio (SNR), the Polarimetric Ratio (PR), and the width of the waveforms' trailing and leading edges. These parameters show sensitivity to the effects of the Earth's topography and Above Ground Biomass (ABG) even over Amazonian and Boreal forests. These effects are shown to be an important factor in precise soil moisture and biomass determination. Additionally, it is found that PR shows sensitivity to soil moisture content over different land cover types. In particular, the following values of the PR are found over: (a) tropical forests ~ -1.2 dB; (b) boreal forests ~ 0.8 dB; (c) Greenland ~ 2.8 dB; and (d) the Sahara Desert ~ 3.2 dB.

Keywords: GNSS-Reflectometry; SMAP; polarimetry; scatterometry; soil moisture; biomass

1. Introduction

The concept of multistatic scatterometry was proposed by Hall and Cordey in 1988 [1]. GNSS-R is an Earth Remote Sensing technique that exploits the signals transmitted by the Global Navigation Satellite Systems and hence can provide a dense global coverage of the Earth's surface with rapid revisit time. It was originally proposed in 1993 by Martin-Neira for mesoscale ocean altimetry [2,3] to improve the spatio-temporal sampling of conventional nadir-looking radar missions. During the last decades, several ground-based [4], airborne, [5] and balloon [6] experiments have been carried out to demonstrate the feasibility of this technique for ocean altimetry and scatterometry. At present, GNSS-R ocean scatterometry applications are quite mature. On the other hand, the bistatic scattering properties over land surfaces deserve further study to evaluate the performance of this technique for soil moisture determination and biomass monitoring.

The first space-borne opportunistic measurement of an Earth-reflected GPS signal took place during the Space-borne Imaging Radar-C (SIR-C) mission in 1994 [7]. The first designed experiment of GNSS Reflectometry from space took place on-board the United Kingdom UK-DMC in 2003 [8].

The UK-TechDemoSat-1 using a Surrey Satellite Technology Ltd. (SSTL) receiver was launched in June 2014, providing useful GPS L1 C/A code data sets for the GNSS-R community [9]. Researchers, have studied the sensitivity of GNSS-R for soil moisture determination [10,11], ocean altimetry [12] and

scatterometry [13,14], and sea ice detection [15]. More recently, the 6U cubesat ³Cat-2 [16] developed by the Universitat Politècnica de Catalunya (UPC) was launched on 15 August 2016, and NASA's Cyclone Global Navigation Satellite System (CyGNSS) GPS L1 C/A code-based constellation was recently launched on 15 December 2016 [17], providing an unprecedented sampling of the Earth's surface.

In 2000, the use of polarimetric GNSS-R was first proposed by Zavorotny for soil moisture determination [18]. At present, there are two main approaches for soil moisture determination with GNSS-R: (i) the first uses tower-based geodetic GNSS receivers and the multipath Signal-to-Noise Ratio (SNR) to retrieve ground moisture [4,19,20] in a small region around the tower; (ii) the second one uses specifically designed receivers and two antennas either at Left and Right Hand Circular Polarizations (LHCP and RHCP) as in [21–23], or at horizontal H and vertical V polarizations as in [24]. The second technique using an horizontal H-Pol and V-Pol antenna is used in this work. Theoretical [25,26] and experimental [27] assessments have shown a sensitivity to forest biomass. Recent airborne [21] and stratospheric balloon [28] flight experiments have been performed using new instruments and circular polarization antennas (RHCP and LHCP) for geophysical parameter retrieval over land surfaces, and wetlands. These experiments have shown the capability of GNSS-R techniques for wetlands monitoring even from high altitude platforms (~27 km) [28] because of the high spatial resolution provided by the coherent component of the scattered field.

This study presents results from a serendipitous GNSS-R experiment performed on-board the SMAP mission [29] over continental areas. This unique data set, which provides very high-gain GPS L2C code dual-polarization (H and V) sampling of the Earth's surface up to high latitudes, is evaluated to assess the behaviour of different parameters of the so-called reflected waveforms corresponding to Soil Water Index (SWI), Normalized Difference Vegetation Index (NDVI), Above Ground Biomass (AGB), and topography. Section 2 describes the methodology and the experiment set-up. Section 3 presents the results, Section 4 provides final discussions, and the main conclusions are highlighted in Section 5.

2. Description of the GNSS-R Experiment

The SMAP mission was successfully launched on 31 January 2015 into a Sun-Synchronous Orbit (SSO) with a local time of ascending node (LTAN) of 6:00 h, and an orbit height of ~685 km. The main mission instruments are an active L-band radar and a passive radiometer which share a ~14 rev/min rotating 6-m aperture reflector antenna scanning a wide 1000 km wide swath (Figures 1 and 2). The dual-polarization reflector (H and V) points to Earth's surface with an approximately fixed elevation angle of $\theta_e \sim 55^\circ$. The elevation angle of the collected signals was approximately constant ~55° during the complete experiment because the attitude of the SMAP satellite is the same in nominal operations. Data acquisition used a 50 km cut on (footprint area ~7800 km²) the closest approach to the specular point, and calibrated using the antenna radiation pattern. This possibly is cutting off the waveform trailing edge over some regions. Figure 3 shows enough sensitivity from Greenland to tropical forests. The High-Power Amplifier (HPA) failed on 7 July 2015, preventing the emission of radar pulses and thus the use of the instrument as an active device. As an experiment of opportunity, the radar receiver was tuned to the GPS L2 frequency (1227.6 MHz) in order to collect Earth-reflected GPS signals. Raw data were downloaded to the ground and then a geometric model was used to select SMAP's Level L1 A binary data (orbit, attitude, antenna pointing, etc.) extraction from their archive to only those time periods with potential specular reflections (Figure 2). These data, combined with GPS orbital information, were used to predict when the SMAP's antenna pointed to a nominal specular reflection point. This timing information was then used by a L1 A Block Floating Point Quantization (BFPQ) for In-phase (I) and Quadrature-phase (Q) conversion, where H-Pol and V-Pol data were extracted. This converter read in SMAP Level 1A data, and converted the compressed BFPQ numbers to I and Q 8-bit signed integers. These I/Q data had continuity gaps when the radar transmitter was supposed to be transmitting. The converter computed the required number of zero-valued samples to be inserted to provide a temporally continuous data set. These continuous I/Q samples were

passed to the GPS L2 acquisition software, which searched in Doppler and delay for the L2 Civilian Medium-length code (L2CM), which repeats every 20 milliseconds. Once this code was found, the software aligned with the L2C Long code (L2CL), which repeats every 1.5 s. The precise Doppler and range information was passed on to the DDM processor, creating Delay Doppler Maps (DDMs) spanning ± 10 kHz in Doppler and ± 3000 km in range, and centered at the strongest detected signal, for both the H and V polarization data. After inspection, the data set was seen to be free of potential effects of Faraday rotation. Two signal peaks were selected because the direct GPS signal was almost always present in the data: timing between the two signals unambiguously determined which was the reflected signal used here. Finally, after averaging, power DDM's $\langle |Y^{\text{ref}}|^2 \rangle$ were obtained as a result [18,30]:

$$\langle |Y^{\text{ref}}|^2 \rangle = \frac{P_t \lambda^2}{(4\pi)^3} \iint \frac{D_T(\vec{\rho}) D_R(\vec{\rho}) |\chi(\tau - (R_0 + R)/c, f_D(\vec{\rho}) - f_c)|^2 \sigma^0(\vec{\rho})}{R_T^2(\vec{\rho}) R_R^2(\vec{\rho})} d^2\rho, \quad (1)$$

where P_t is the transmitted power, D_T and D_R are the transmitter and receiver antenna directivities at the point $\vec{\rho}$ over the Earth's surface, R_T and R_R are the distance from the transmitter and the receiver to point $\vec{\rho}$, $|\chi(\tau, f)|^2$ is the Woodward Ambiguity Function (WAF), and σ^0 is scattering coefficient. The coherent integration time was set to $T_{\text{coh}} = 5$ ms and the number of incoherent averaging $N_{\text{inc}} = 5$ to increase the Signal-to-Noise Ratio (SNR). Lower levels of T_{coh} were tested, and it was found that $T_{\text{coh}} = 5$ ms is the optimum for this experiment configuration. The spatial resolution associated to the waveforms' peak is linked to the first Fresnel zone (~ 1 km²) in the case of specular scattering, and limited by the glistening zone in the case of the non-specular scattering, related to the area of the first iso-delay ellipse, that is ~ 1800 km²; plus the degradation due to: (a) the platform's movement (in the SMAP's case this degradation is $|\vec{v}_{\text{SMAP}}| \cdot T_c \cdot N_{\text{inc}} = 7.48$ km/s \cdot 0.005 s \cdot 5 = 0.187 km); (b) the antenna rotation; this degradation is unique to this scenario, and as a consequence the point at antenna boresight moves ~ 18 km during the integration time.

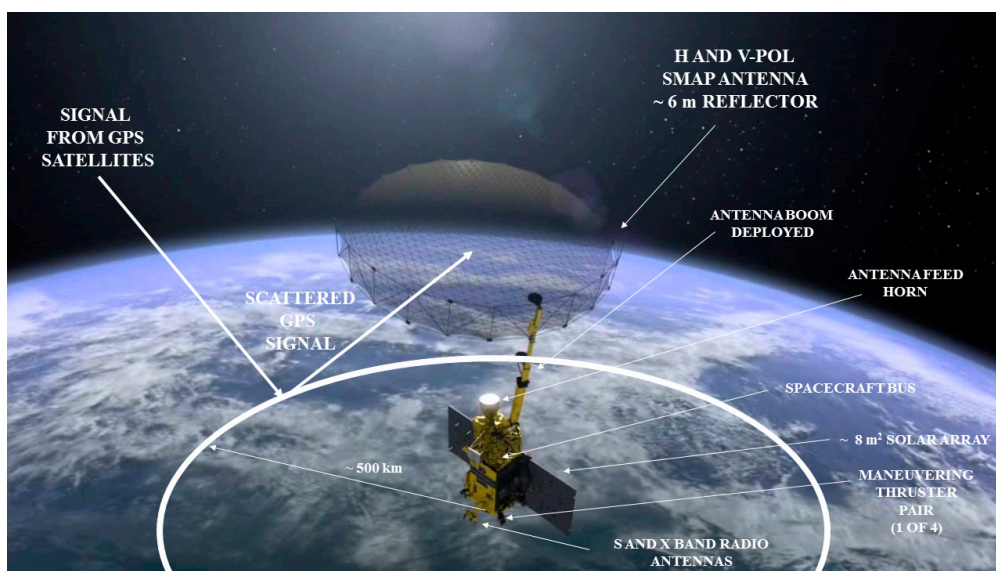


Figure 1. The Soil Moisture Active Passive (SMAP) mission was successfully launched on 31 January 2015 into a Sun-Synchronous Orbit (SSO) with a local time of ascending node (LTAN) of 06:00 h, and an orbit reference height of ~ 685 km. The experiment set-up of the Global Navigation Satellite Systems Reflectometry (GNSS-R) experiment on-board the SMAP mission is represented in this figure. Scattered GPS signals were collected by the SMAP's radar antenna at an elevation angle $\theta_e \sim 55^\circ$. The gain of the H-Pol and V-Pol antenna was ~ 36 dB. Data processing was performed on-ground at NASA's Jet Propulsion Laboratory (JPL).

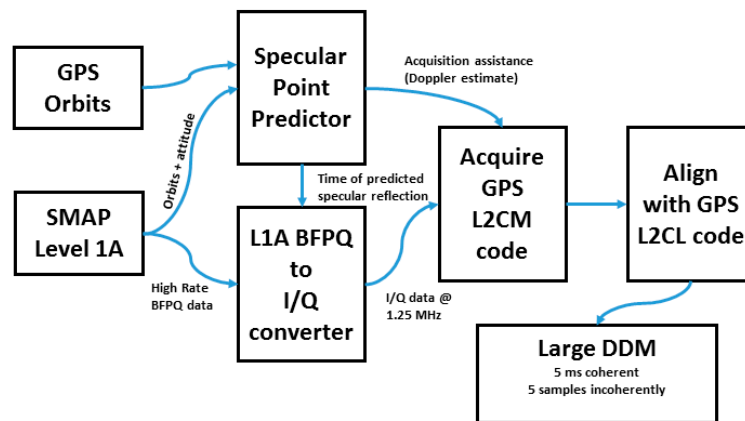


Figure 2. Signal processing chain to convert SMAP Level 1A “high rate” data to Delay Doppler Maps (DDMs). The SMAP orbit, attitude, and antenna pointing are used to predict times when specular reflections will be visible. These “high rate” data is filtered by these times, and only relevant portions converted to I/Q for GPS L2C DDM generation.

Waveforms corresponding to the Doppler central frequency were obtained for further assessment over land and cryosphere. Averaged waveforms with the associated RMS at each lag are represented in Figure 3 for both polarizations and different terrain types. To describe the shape of the waveforms quantitatively and to account for the power differences and spreading of the signal, the following parameters are used: Signal-to-Noise Ratio (SNR), Polarimetric Ratio (PR), and waveforms’ trailing and leading edges width.

The SNR is estimated as in [31], and defined as [3]:

$$\text{SNR} = \frac{\langle |Y^{\text{ref}}|^2 \rangle}{\langle |Y^{\text{noise}}|^2 \rangle} = \frac{\langle |Y^{\text{ref}}|^2 \rangle}{k_B T B}, \quad (2)$$

where k_B is the Boltzmann constant, T is the equivalent noise temperature of the down-looking chain, and B is the signal bandwidth.

The Polarimetric Ratio (PR) is computed to properly evaluate the fluctuations of the dielectric properties of scatterers, since theoretically it can cancel out the effects of soil surface roughness without biomass [18], although it does not do so perfectly for arbitrary scattering media. The PR at linear polarization is high when soil moisture content is weak and reversely. On the other hand, at circular polarization the ratio increases with the moisture [18]. It is estimated as the ratio of the peak of the reflected signal power waveform at H-Pol over the peak of the reflected signal power waveform at V-Pol, after proper compensation of the noise power floor and the antenna radiation pattern:

$$\text{PR} = \frac{\langle |Y_H^{\text{ref}}|^2 \rangle}{\langle |Y_V^{\text{ref}}|^2 \rangle}. \quad (3)$$

The theoretical definition of the PR is provided in [32] as:

$$\text{PR} = \sigma_H / \sigma_V, \quad (4)$$

where σ_H and σ_V are the bistatic radar cross-sections of H and V respectively.

Over land surfaces, there are two contributions to the waveforms: coherent and incoherent scattered fields in different proportions. In this scenario, the Kirchhoff Approximation in the Physical

Optics Approximation (KPO) provides a reasonable theoretical framework to analyze the results in regions without biomass. The incoherent bistatic scattering coefficient as provided by the KPO is [33]:

$$\sigma_{qp}^{0,inc} = (|a_0|kl/2)^2 e^{-q_z^2 \sigma^2} \sum_{n=1}^{\infty} \frac{(q_z^2 \sigma^2)^n}{n!n} e^{-\frac{(q_x^2 + q_y^2)^2}{4n}}, \quad (5)$$

where $k = \frac{2\pi}{\lambda}$, l is the surface correlation length, σ is the surface height standard deviation, and \vec{q} is the bistatic scattering coefficient. In the specular direction, the coefficient a_0 can be computed for the co-polar component H:

$$a_{0,H} = -2R_H(\theta_{inc}) \cos \theta_{inc}, \quad (6)$$

and for the co-polar component V:

$$a_{0,V} = 2R_V(\theta_{inc}) \cos \theta_{inc}, \quad (7)$$

where θ_{inc} is the incidence angle, and R_H and R_V are the Fresnel reflection coefficients at H-Pol and V-Pol respectively:

$$R_H = \frac{\sqrt{1 - \sin^2(\theta_{inc})} - \sqrt{\epsilon_r - \sin^2(\theta_{inc})}}{\sqrt{1 - \sin^2(\theta_{inc})} + \sqrt{\epsilon_r - \sin^2(\theta_{inc})}}, \quad (8)$$

and

$$R_V = \frac{\epsilon_r \sqrt{1 - \sin^2(\theta_{inc})} - \sqrt{\epsilon_r - \sin^2(\theta_{inc})}}{\epsilon_r \sqrt{1 - \sin^2(\theta_{inc})} + \sqrt{\epsilon_r - \sin^2(\theta_{inc})}}, \quad (9)$$

where ϵ_r is the dielectric constant. For the cross-polar components HV and VH, $a_0 = 0$ [33]. Therefore, upon substitution of (5), (6) and (7) in (4), the Polarimetric Ratio is found to be independent of the surface roughness:

$$PR = \frac{R_H}{R_V}. \quad (10)$$

In the case of the coherent component of the scattered field [33] (p. 1008), the PR is obtained as the ratio of the H reflectivity over the V reflectivity as:

$$PR = \frac{\Gamma_H}{\Gamma_V} = \frac{|R_H|^2 e^{-(2\sigma k \cos \theta_{inc})^2}}{|R_V|^2 e^{-(2\sigma k \cos \theta_{inc})^2}}, \quad (11)$$

Equation (11) shows that in the case of the coherent scattering, the PR is also theoretically independent of the soil surface roughness because the surface height standard deviation is independent of the signal polarization.

The width of both edges was defined as the lag difference between the 30% and the 100% of the maximum power of the waveform (Figure 4). Finally, it is highlighted that the generated SMAP GNSS-R dataset provided a unique opportunity for research in GNSS-R, despite this mission being designed for a different goal, because the SMAP's radar receiver allowed the collection of reflected GNSS signals at L2, through the use of a high gain antenna ~ 36 dB. The observables (SNR, PR, and trailing and leading edges) will be used to analyze the reflected waveforms (Figure 3). In this figure, significant differences are seen among different areas. One of the most surprising results is the large spreading of the waveforms over Greenland and the large SNR over the Sahara Desert. These points will be further discussed in Section 3.

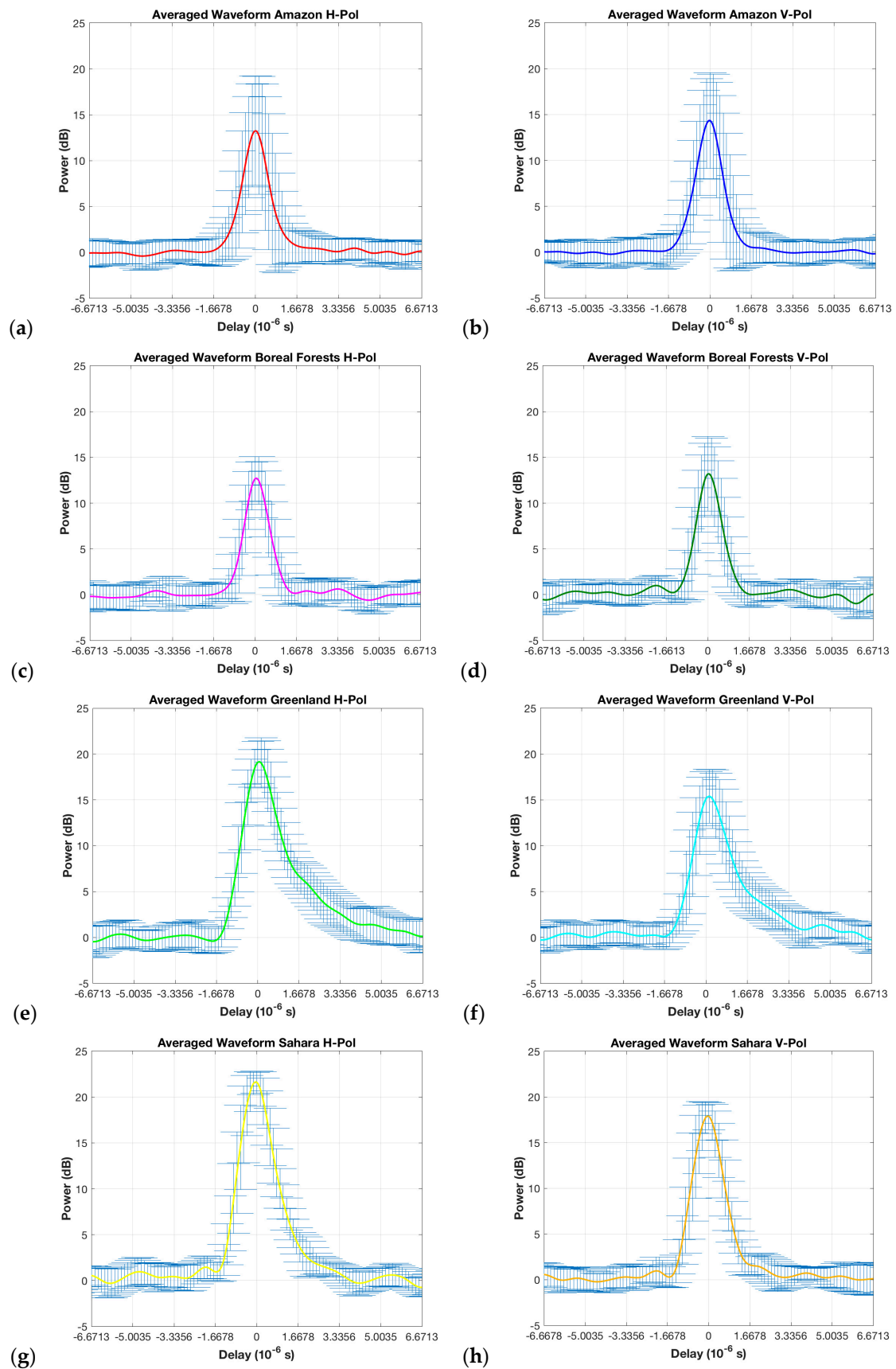


Figure 3. One-day (~100 samples) averaged power waveforms [$T_{coh} = 5$ ms and $N_{inc} = 5$] over selected target areas: (a) H-Pol Amazon; (b) V-Pol Amazon; (c) H-Pol boreal forests; (d) V-Pol boreal forests; (e) H-Pol Greenland; (f) V-Pol Greenland; (g) H-Pol Sahara; and (h) V-Pol Sahara.

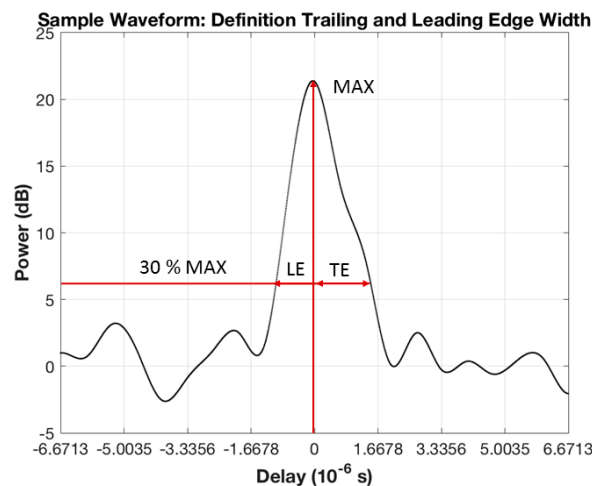


Figure 4. Definition of the trailing and leading edge width over a sample waveform.

3. Earth Surface Effects on GNSS-R Relevant to Land Applications

The potential of spaceborne GNSS-R for land applications is evaluated, first at a global scale and then at a regional scale. The results are displayed in a 0.1° latitude/longitude grid with a 1° pixel size used in the spatial averaging, performed with steps of 0.1° . The total number of observations over land surfaces is $\sim 35,000$ per month ($\sim 70,000$ considering direct and reflected signals), and the maps are constructed using a mean value of $\sim 25 \pm 4$ measurements per pixel. There are more data availability over target areas at larger latitude than over the equator because of the SMAP's orbit parameters (polar orbit). On the other hand, the area of the selected pixel size gradually reduces from the equator to the poles. The lat/lon grid was selected to homogenize the number of measurements per pixel. In the close up over Africa, the selected spatial averaging size was 2° , also performed with steps of 0.1° . The pixel size was selected to be larger than that of global averaged maps because of the of lower data availability. The waveforms' parameters (SNR, PR, and trailing & leading edges) are geo-located over the specular points on the Earth's surface. Four different relatively "homogeneous" areas are considered to study statistically the waveforms' properties associated with different scattering mechanisms. In particular, the coordinates of these regions are: (a) tropical forests: latitude = $(-3, 3)^\circ$ by longitude = $(15, 25)^\circ$; (b) boreal forests: latitude = $(50, 70)^\circ$ by longitude = $(90, 140)^\circ$; (c) Greenland: latitude = $(75, 83)^\circ$ by longitude = $(-53, -31)^\circ$; and (d) Sahara Desert: latitude = $(19, 28)^\circ$ by longitude = $(-7, 27)^\circ$. Four different three-months seasons (January–March, April–June, July–September, and October–December) have been selected to analyze the effect of seasonal variations at a regional scale on soil moisture and vegetation water content.

3.1. Global Scale

The global one-year averaged maps (1 September 2015 to 1 September 2016) provided in this study are useful for the global scale study. Signal-to-Noise Ratio (SNR) values are presented for H-Pol and V-Pol respectively in Figure 5a,b over the Earth's land surface. High SNR peaks correspond to bare soil regions with high soil moisture content such as the Pampas of Argentine, the Great Lakes regions in the US, Northern India, or the Northern Yakutia region in Russia. There are also high power peaks over regions such as the Sahara Desert despite the low soil moisture values. This effect will be investigated at a regional scale. In regions with significant amount of AGB, the SNR values are lower despite high values of soil moisture content because of the effect of signal attenuation (Figure 5a,b). The PR values (Figure 5c) show good correlation (Pearson linear correlation factor $r \sim -0.6$) to soil moisture content by comparing them to SMAP's radiometer data (Figure 5d). It appears higher PR values are associated with larger waveform spreading (Pearson linear correlation factor $r \sim 0.4$). These results are clearly illustrated in Figures 5c and 6a–d. In regions with higher PR and little vegetation

(Greenland, Australia, the Sahara Desert, the Gobi Desert, the Arabian Desert, and the Kalahari Desert) waveform spreading is larger than regions with higher values of above ground vegetation (Amazonian and Boreal forests), and lower waveform spreading.

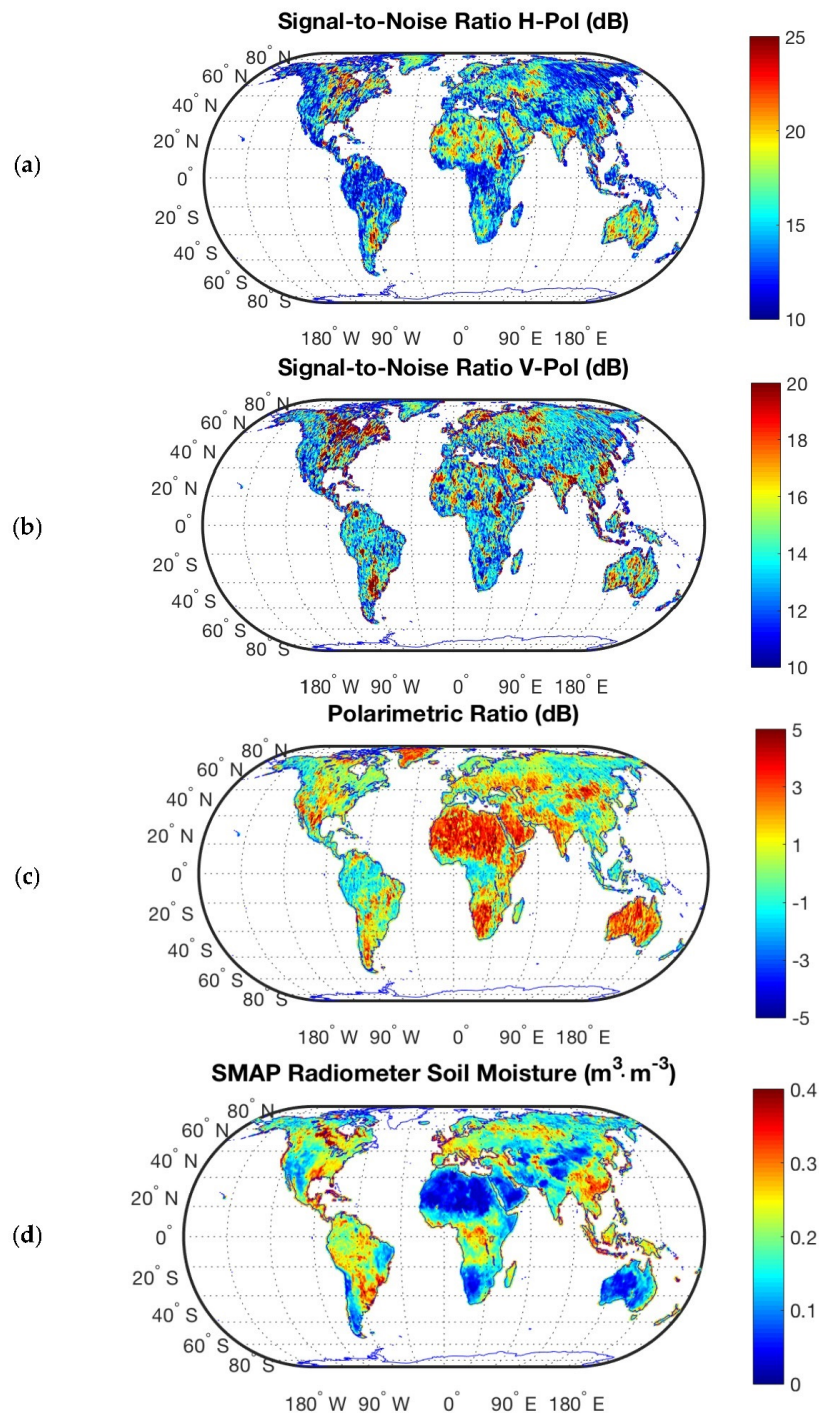


Figure 5. SMAP over-land power waveform analysis using one-year averaged values: (a) Signal-to-Noise Ratio H-Pol [dB]; (b) Signal-to-Noise Ratio V-Pol [dB]; (c) Polarimetric Ratio [dB]; (d) Global distribution of time-averaged retrieved surface soil moisture based on SMAP radiometer observations and application of the multi-temporal dual-channel algorithm by Piles et al [34,35]. Volumetric soil moisture measured for the first few centimeters (in fact the penetration depth depends on the soil mineralogical content and the moisture).

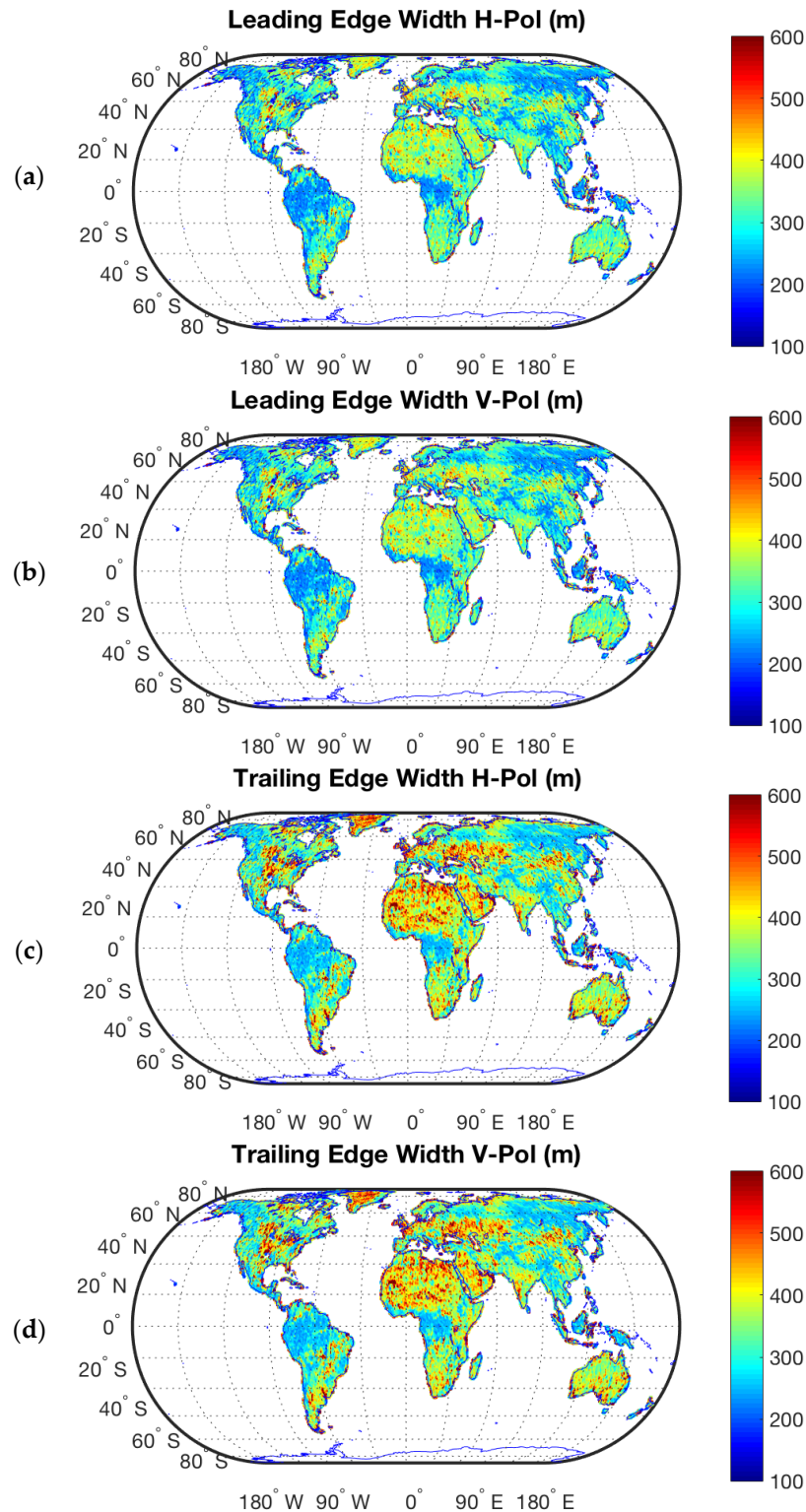


Figure 6. SMAP over-land power waveforms shape analysis: (a) leading edge width H-Pol [m]; (b) leading edge width V-Pol [m]; (c) trailing edge width H-Pol [m]; and (d) trailing edge width V-Pol [m].

For a given elevation angle, the level of signal depolarization depends on the surface roughness, and the scatterer type through the scattering coefficient σ^0 . Therefore, the SMAP data set, which has an approximately constant elevation angle of $\theta_e \sim 55^\circ$, is useful to analyze the GNSS-R sensitivity to

changes in the dielectric constant. Figure 5c shows the good sensitivity of the PR for different levels of Above Ground Biomass (ABG), from ~ 100 ton/ha for boreal forests to ~ 350 ton/ha for tropical rainforests (Figure 7a). The transitions zones from arid to dense vegetation areas are well represented in Africa and Asia from the North to the South. Over dense vegetation areas, the PR takes negative values, which suggests that the vertical stalks scatter more vertically polarized waves. These maps show that this observable depends on dielectric and scattering property changes over biomass and wetlands (see Amazon river and lakes regions). This is the reason that explains the behaviour in Figure 8a,b where there are two types of waveforms: those with higher power levels corresponding to areas over the Amazon river and riparian forest, and those corresponding only to tropical forests with lower power level because of signal attenuation [11,36]. The attenuation due to vegetation is $L^{\text{canopy}} = e^{\tau^{\text{canopy}} / \cos \theta_{\text{inc}}}$, where τ^{canopy} is the nadir optical depth of the vegetation layer [11]. Over the Amazon river and riparian forests the SNR ranges from ~ 15 dB to ~ 30 dB depending on the proportions of land signal contamination. The highest power waveforms' peaks are even stronger than over Greenland because of the specular reflection over smooth and calm water. However, the averaged waveform shows a higher peak power over Greenland than over the Amazon region and a dissymmetric shape (Figure 3). In South America, when the specular point moves away from the tropical forests, the spreading of the waveforms increases, also showing detectability to the Amazon river with a higher PR value (Figure 5). Furthermore, it is also observed that the spreading of the trailing edge is larger than the leading edge. This aspect over tropical rainforests will be further evaluated at a regional scale.

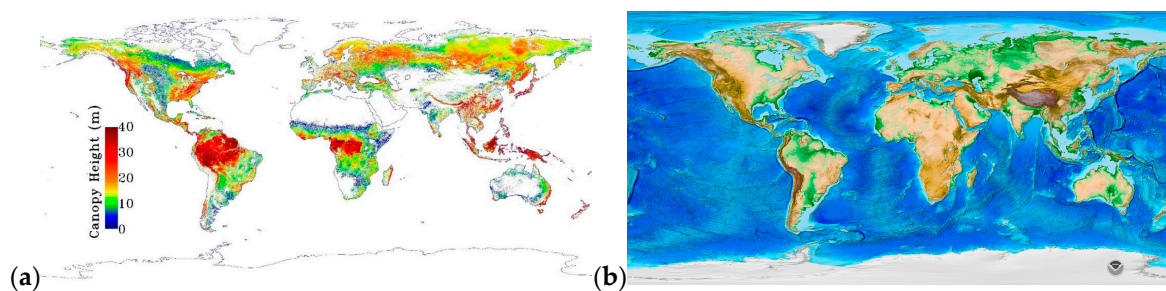


Figure 7. (a) Global map of forest height produced from NASA's ICESAT/GLAS, MODIS, and TRMM sensors. Available online: <https://www.nasa.gov/topics/earth/features/forest20120217.html>. (b) ETOPO1 Global Relief Model. Available online: <https://www.ngdc.noaa.gov/mgg/global/global.html>.

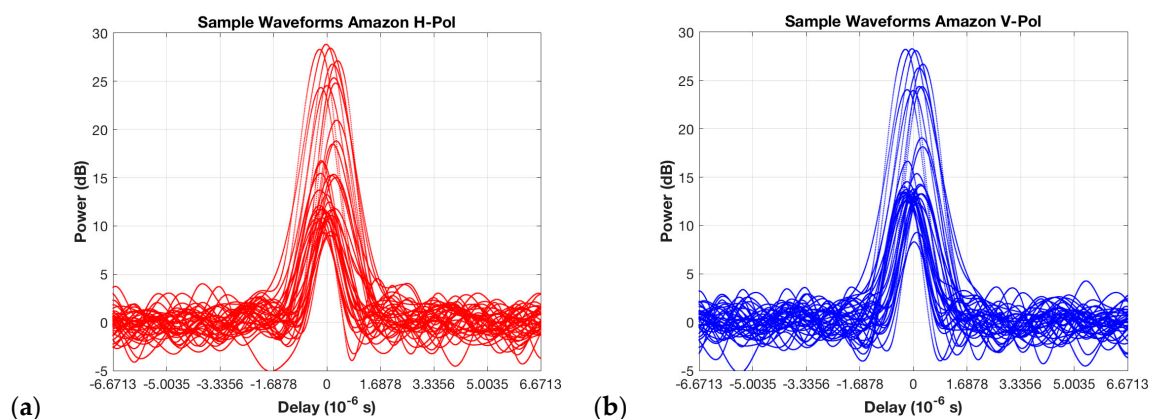


Figure 8. Sample power waveforms [$T_{\text{coh}} = 5$ ms and $N_{\text{inc}} = 5$]: (a) H-Pol Amazon; (b) V-Pol Amazon.

The topography [11] is a key parameter to take into consideration, in addition to the effects of biomass, because the scattering coefficient σ^0 is proportional to the probability that a facet could forward scatter the electromagnetic field to the receiver in a specular way. AGB over some areas

of the Himalayas is ~200 ton/ha [37], so that both effects (topography and biomass) are merged. Looking at the East mountains of Greenland and the Andes mountains (Figure 7b), neither with appreciable vegetation (Figure 7a), it can be seen that topography contributes to the GNSS signals depolarization (Figure 5c). The effect of topography is further analyzed using the information on the waveforms leading and trailing edges width (Figure 6). Similar measurements of waveform spreading were obtained for H-Pol and V-Pol. At regional scale H-Pol is selected for further study. Similar antenna gain and rate of change of the radar cross-section with the positioning vector, at both polarizations. These observables are used here for the first time (to the authors' knowledge) for land surfaces applications. In particular, the width of both edges is assessed as a function of the surface type. It is shown that there is a dependence on changes in topography but also in dielectric properties. The width is lower for larger values of biomass and surface topography. This result deserves attention since, in this case, a lower spreading of the waveforms does not mean a higher signal coherence. In the latter case, it means that the area that contributes to the signal in the specular direction is reduced. In the former case, the interpretation is that the effects of attenuation are very strong away from the nominal specular reflection point so that the spreading of the waveform is lower as compared to bare soil.

Finally, this reconstructed SNR at Left Hand Circular Polarization is also shown here for reference (Figure 9) as [32]:

$$\text{SNR}_{\text{LHCP}} = \left(\frac{\sqrt{\text{SNR}_H} + \sqrt{\text{SNR}_V}}{2} \right)^2 \quad (12)$$

Figure 9 shows high peaks power associated with bare regions with high soil moisture values, lakes regions and also over the Sahara Desert (black rectangles in Figure 9). On the other hand, lower power levels are observed over tropical or boreal forests due to the larger signal attenuation.

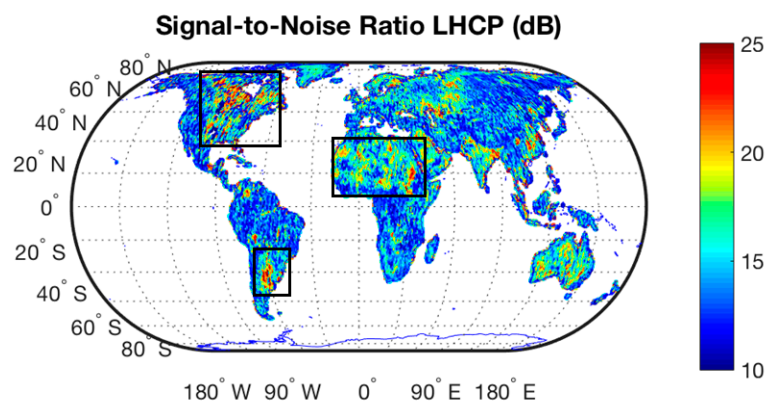


Figure 9. SMAP over-land Signal-to-Noise Ratio at LHCP [dB] using one-year averaged values.

3.2. Regional Scale

This section provides a regional scale analysis (Figure 10) with focus on Africa-Congolian tropical rainforests, Sahara and Kalahari Desert (Figures 11–13), Northern Asia Boreal forests (Figures 14–16), and the Greenland ice sheet (Figures 17 and 18). These three regions have been selected because they provide a wide overview of different scattering properties over the Earth's surface. The information provided by the seasonal variations of the PR, SNR, and the spreading of the waveforms is complemented with maps of Soil Water Index (SWI) from METOP-ASCAT [38], and Normalized Difference Vegetation Index (NDVI) from MODIS [39]. Additionally, the effect of larger AGB on tropical rainforests as compared to boreal forests is derived from the lower levels of SNR for higher AGB, the lower PR, and the lower spreading of the waveforms, as compared to different terrain types (Figure 10).

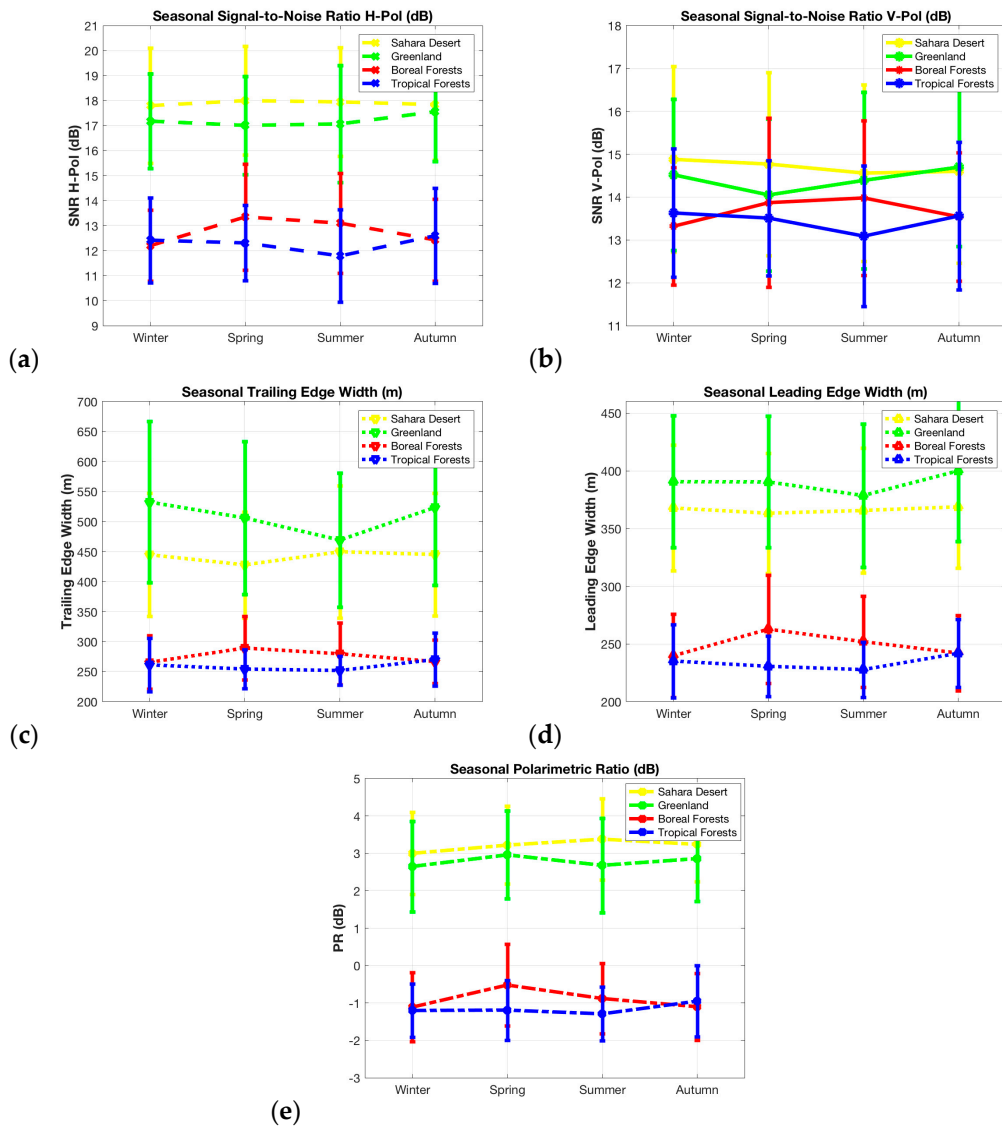


Figure 10. Annual evolution (mean and standard deviation) of main waveforms' parameters: (a) Signal-to-Noise Ratio H-Pol (dB); (b) Signal-to-Noise Ratio V-Pol (dB); (c) trailing edge width (m); (d) leading edge width (m); and (e) Polarimetric Ratio (dB).

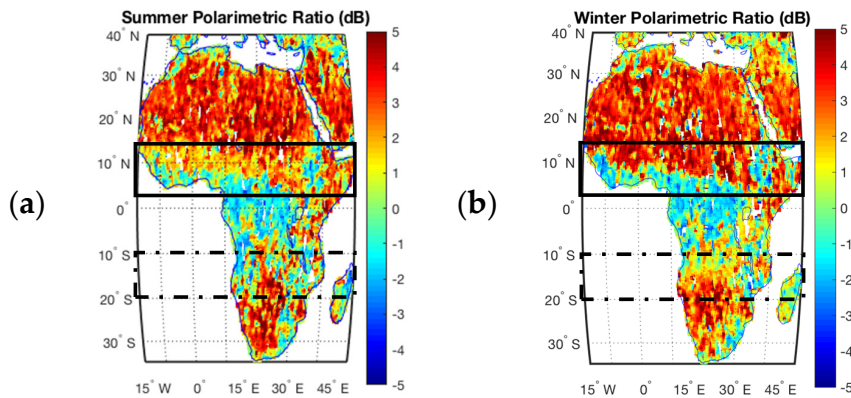


Figure 11. Cont.

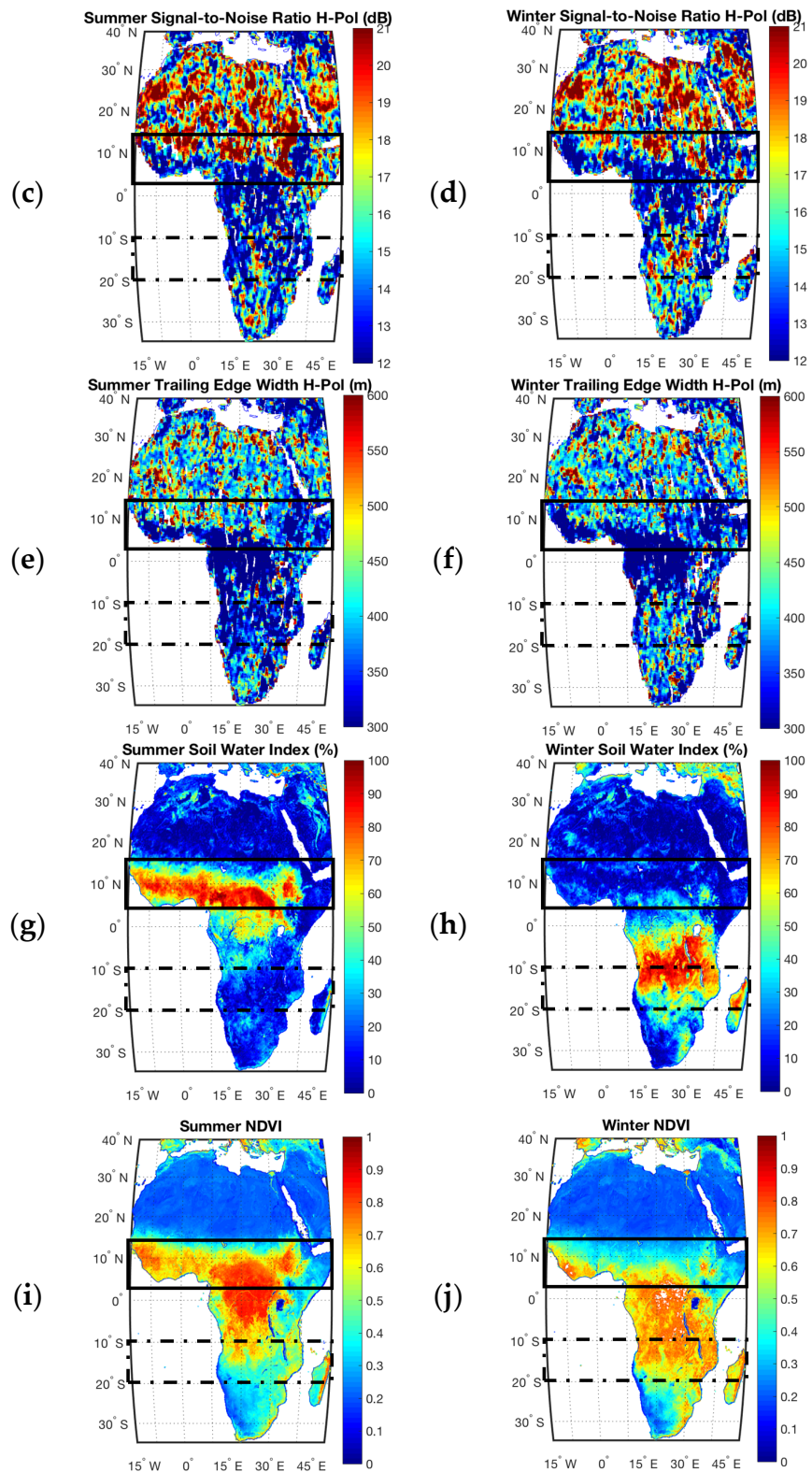


Figure 11. Regional study over Africa. Polarimetric Ratio (a) Summer; (b) Winter. Signal-to-Noise Ratio (c) Summer; (d) Winter. Trailing edge width (e) Summer; (f) Winter. Soil Water Index (g) Summer; (h) Winter. Normalized Difference Vegetation Index. (i) Summer; (j) Winter.

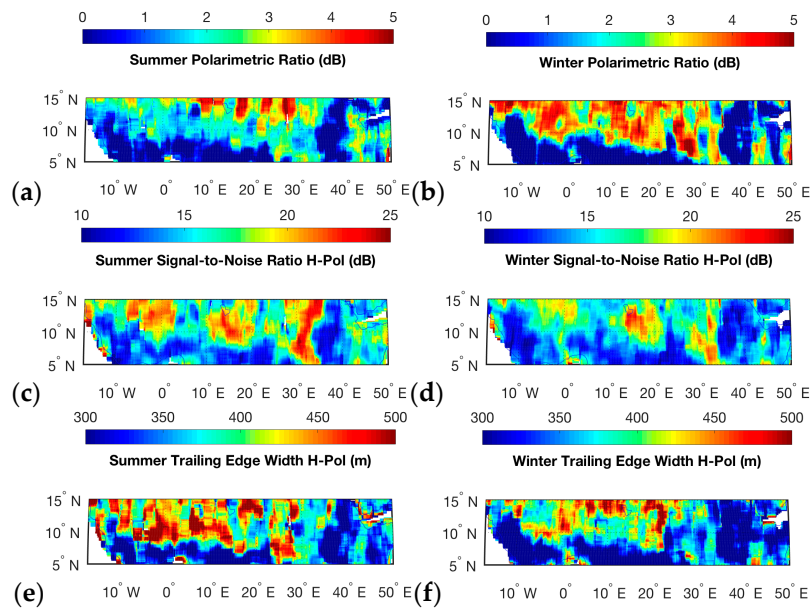


Figure 12. Close up over Northern Africa. Polarimetric Ratio (a) Summer; (b) Winter. Signal-to-Noise Ratio (c) Summer; (d) Winter. Trailing Edge Width (e) Summer; (f) Winter.

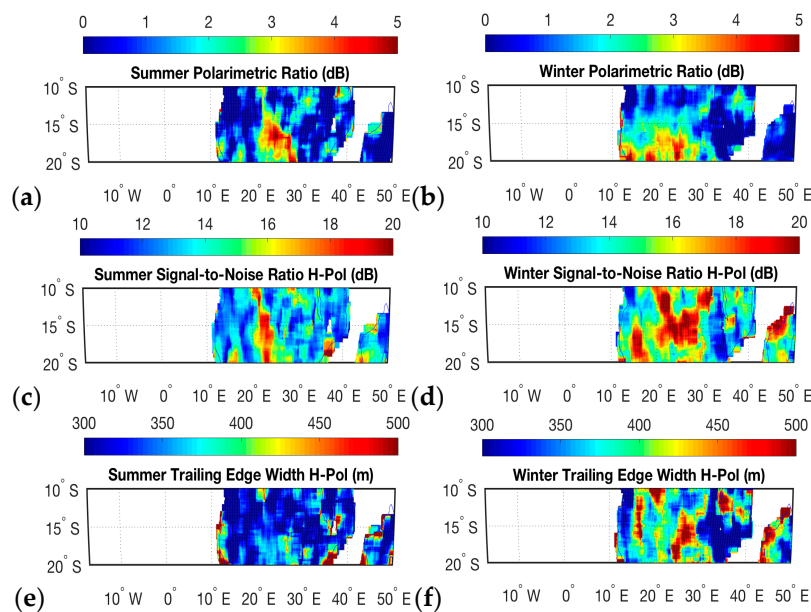


Figure 13. Close up over Southern Africa. Polarimetric Ratio (a) Summer; (b) Winter. Signal-to-Noise Ratio (c) Summer; (d) Winter. Trailing Edge Width (e) Summer; (f) Winter.

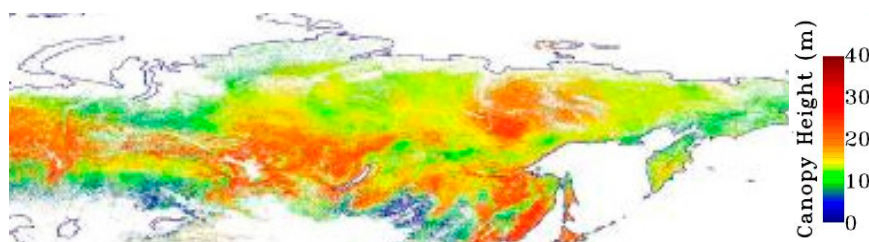


Figure 14. Map of forest height over Northern Asia produced from NASA’s ICESAT/GLAS, MODIS, and TRMM sensors.

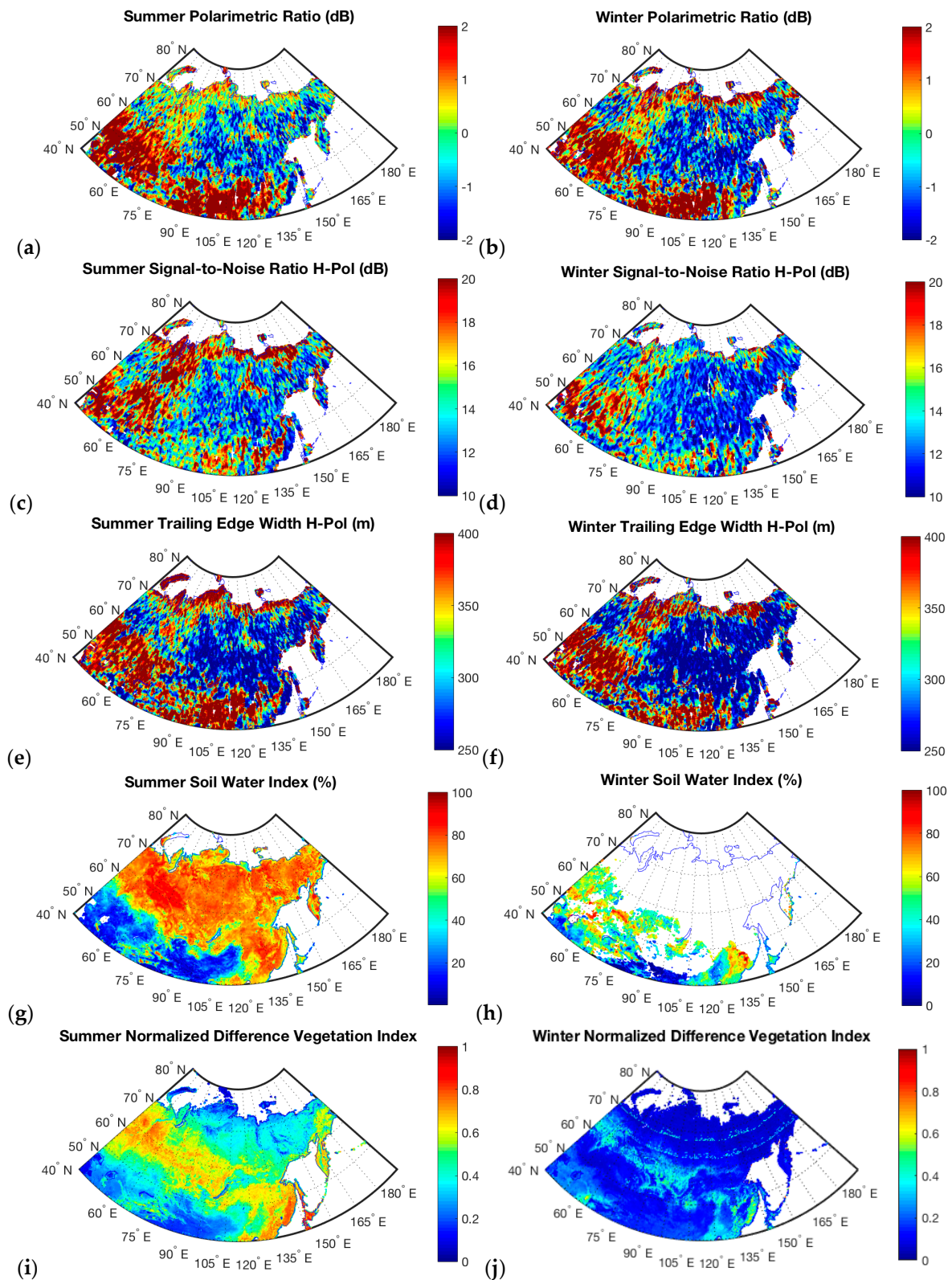


Figure 15. Regional study over Northern Asia. Polarimetric Ratio (a) Summer; (b) Winter. Signal-to-Noise Ratio (c) Summer; (d) Winter. Trailing edge width (e) Summer; (f) Winter. Soil Water Index (g) Summer; (h) Winter. Normalized Difference Vegetation Index. (i) Summer; (j) Winter.

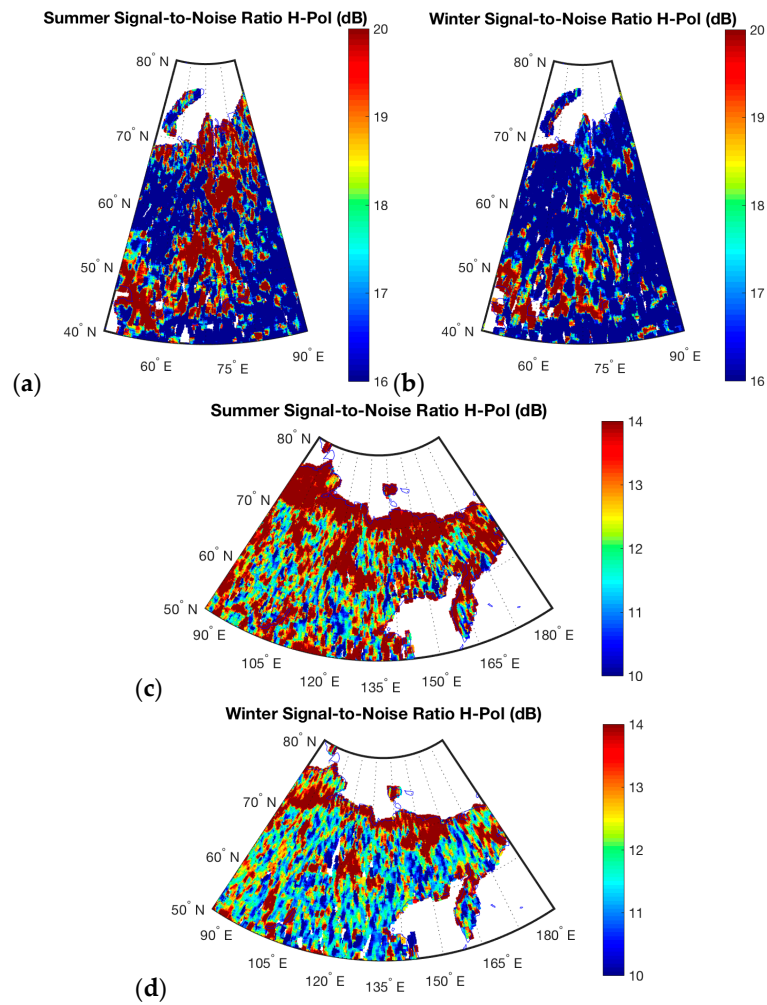


Figure 16. Close up of Signal-to-Noise Ratio seasonal changes over central Russia: (a) Summer; (b) Winter; and over Eastern Russia: (c) Summer; and (d) Winter.



Figure 17. View of the extent and frequency of surface melt for the Greenland ice sheet. Data from the National Snow and Ice Data Center.

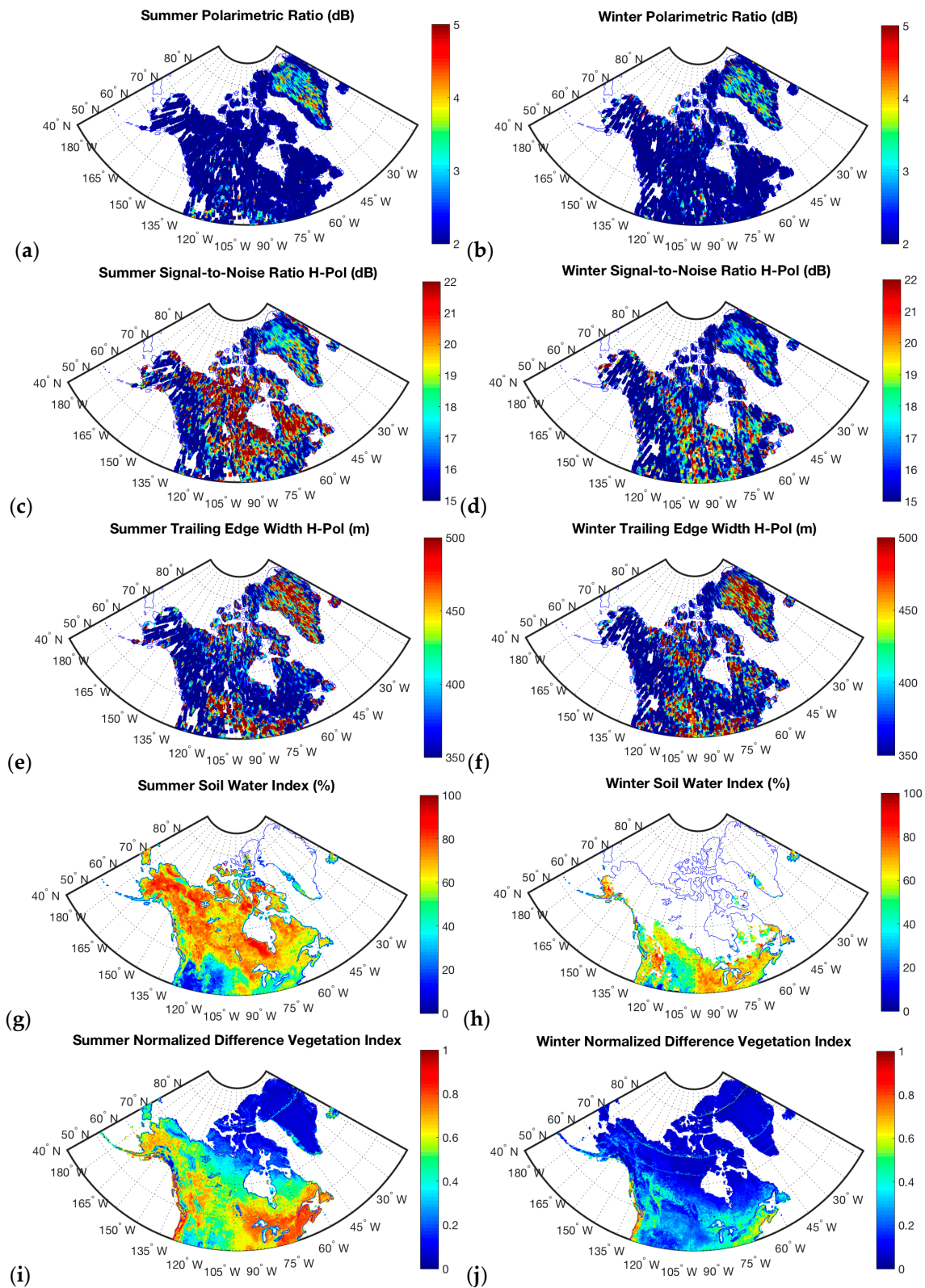


Figure 18. Regional study over North America and Greenland. Polarimetric Ratio (a) Summer; (b) Winter. Signal-to-Noise Ratio (c) Summer; (d) Winter. Trailing edge width (e) Summer; (f) Winter. Soil Water Index (g) Summer; (h) Winter. Normalized Difference Vegetation Index; (i) Summer; (j) Winter.

3.2.1. Africa: Arid Deserts and Congolian Rainforests

Over bare soil, the scattering is mainly related to surface scattering, being driven by the soil moisture and surface roughness. However, the high spatial variability of the SNR over the Sahara Desert could be explained by both surface (Rocky Mountains, boulder and graves zones, and sand seas) and subsurface scattering contributions as Camps suggested for first time in [11]. Volume scattering could occur under dry conditions allowing the GNSS signals to penetrate the subsurface [40–42] for rich sand content areas. This could explain the large SNR values over the Sahara despite the low soil moisture (Figure 11c,d). On the other hand, the large waveform spreading (Figure 11e,f) over the Sahara Desert is difficult to be attributed to this geophysical effect because of the low penetration depth around (~2 m) for 0% of volumetric moisture content at L band. The effect of the sand seas (that continuously reshape the surface) on the scattering coefficient, should be considered as a plausible reason, particularly the dunes, which show the characteristics of the sand and the long-term wind [43]. Additionally, almost negligible seasonal variations over the Sahara are observed since SWI (Figure 10g,h) and NDVI are nearly constant during the year in this region (Figure 11i,j).

Seasonal fluctuations over Africa are found in the latitude ranges from $\sim 9^\circ$ to $\sim 15^\circ$, and from $\sim -20^\circ$ to $\sim -10^\circ$, where the geophysical parameters changes are large from Summer to Winter (SWI in Figure 11g,h, and NDVI in Figure 11i,j). Seasonal variations of the Polarimetric Ratio ($PR_{\text{Summer}} \sim 1$ dB in Figure 12a vs. $PR_{\text{Winter}} \sim 4$ dB in Figure 12b) are anti-correlated to changes in SWI, and NDVI. On the other hand, seasonal variations at H-Pol in the SNR ($SNR_{\text{Summer}} \sim 22$ dB in Figure 12c & $SNR_{\text{Summer}} \sim 13$ dB in Figure 13c vs. $SNR_{\text{Winter}} \sim 18$ dB in Figure 12d & $SNR_{\text{Winter}} \sim 17$ dB in Figure 13d), and the trailing edge width ($TE_{\text{Summer}} \sim 460$ m in Figure 12e & $TE_{\text{Summer}} \sim 340$ m in Figure 13e vs. $TE_{\text{Winter}} \sim 390$ m in Figure 12f & $TE_{\text{Winter}} \sim 440$ m in Figure 13f) are correlated to changes in SWI and NDVI. This could be explained since the larger scattering coefficient over the soil, associated with larger SWI, increases the SNR and waveforms spreading, while the larger NDVI attenuates H-Pol signals more than V-Pol signals (Figure 5a,b). The spreading of the waveforms in the latitude range from $\sim 9^\circ$ to $\sim 15^\circ$ (Figure 11e,f) is similar to that over the Sahara Desert, with very low levels of NDVI. However, as it is shown over the equatorial region, the spreading is significantly reduced because of the effect of the Congolian forests with an AGB ~ 350 ton/ha. This suggests that the canopy height (Figure 7a) plays a more important role than the NDVI in the shape of the reflected waveforms. In fact, the SNR is larger over the Sahara and Kalahari Desert than over Congolian forests despite the larger SWI, because the larger signal attenuation due to the larger AGB (Figure 7a). In regions with lower levels of canopy height, the Polarimetric Ratio is more sensitive to changes in NDVI (Figures 7a, 12a,b, and 13a,b).

3.2.2. Asia: Arid Deserts and Boreal Forests

The evaluation over the Northern Asia region is useful to study separately the effects of SWI and AGB (Figures 14–16). The comparison between Figures 14 and 15 shows the effects of higher AGB on the waveforms' parameters, for relatively homogeneous SWI conditions at latitudes higher than $\sim 55^\circ$ (Figure 15g). SWI data from ASCAT could have some limitations for high vegetation density because measurements are derived using a radar operating at a high frequency ~ 5.2 GHz (C-band). The trailing edge width is lower (Figure 15e,f) over regions with higher canopy height (Figure 14), and rapidly increases over the Gobi Desert or over the highest latitudes in Siberia. On the other hand, the highest PR values (Figure 15a,b) and SNR values (Figure 15c,d) are associated to regions with larger values of the trailing edge width (Figure 15e,f). As is shown in Figure 15g–j, NDVI is not associated with SWI over Northern Asia in Winter or Summer. Canopy height (Figure 14) is a key parameter. The spreading of the waveforms, the PR, and SNR values show approximately a similar trend in Summer (Figure 15a,c,e) and Winter (Figure 15b,d,f), but different absolute values. The main difference is the smaller waveforms' spreading in areas with higher values of AGB. Additionally, the SNR is lower in Winter (Figure 16), particularly over areas with lower AGB values, because of the effect of snow on the surface at these latitudes. This additional signal attenuation explains the lower spreading

of the signals in Winter, since a smaller region around the nominal specular point contributes to the power waveforms. Finally, it is found that PR is lower in Summer over Northern Siberia (in agreement with Figure 12) because of the high soil moisture level in Summer (Figure 15g) and snow conditions in Winter (Figure 15h).

3.2.3. North America and Greenland: Lakes Region and Ice Cap

GNSS-R applications can be extended to the study of snow and ice [44–46]. The signal wavelength (λ) at L2 is $\lambda \sim 24$ cm, which is much longer than that radiometers operating at different frequency bands such as AMSR-E and AMSR-2. The wavelength is larger than the grain size and even the snowpack thickness. As a consequence, the medium can be assumed to be homogeneous so that the scattering is determined by the local density fluctuations. At this frequency, ice has a very low absorption coefficient and the refractive index is small. The penetration depth and the scattering coefficient depend on frequency and snow properties. In the case of dry snow, the penetration depth is expected to be around hundreds of meters and therefore the GNSS-R technique is potentially optimum for subsurface studies [47]. On the other hand, the penetration depth of GNSS signals over sea ice is <1 m [48].

Extended regions of Antarctica and Greenland are affected by melting effects (e.g., Figure 17). A recent study [49] additionally shows areas alternatively frozen and thawed in Greenland's inner ice cap (magenta line in Figure 17). Greenland is a focus region of this study (Figure 18). Firstly, it is noted that over bare soil the scattering is significantly determined by soil moisture and surface roughness. However, over dry ice, volume scattering [50], and scattering at different layers [44] could occur allowing the GNSS signals to penetrate the subsurface. The larger waveform spreading over Greenland (Figure 18e,f) could be attributed to this geophysical reason. The effect of subsurface scattering is to increase the waveforms' peak power (Figure 18c,d) and the signals' spreading [50], in agreement with Figure 3e,f. At the same time, in the frame of this work, the large SMAP's antenna gain ~ 36 dB partially compensates the signal attenuation. Therefore, the sensitivity to penetrating signals as seen by SMAP is large as compared to satellites with smaller antennas. Figure 18 shows high values of SNR $\sim (18, 22)$ dB, PR $\sim (3, 5)$ dB, and trailing edge width $\sim (500, 600)$ m over areas in the inner ice cap. However, the waveforms parameters (SNR, PR, and trailing edge) take alternatively low and high values over these areas. On the other hand, the parameters levels are qualitatively similar to those over outer Greenland (see melting effects in Figure 17). Additionally, the width of the waveforms' trailing edge over Greenland increases from Summer (Figures 10 and 18e) to Winter (Figures 10 and 18f) when the weather is colder and the amount of dry ice increases, and therefore the penetration depth would be larger. This waveform data is consistent with the waveforms spreading being due to subsurface scattering effects.

Over North America, it is found that during Summer there are regions with high SNR values corresponding to areas with lakes and high SWI (Figure 18g). During Winter, these power peaks are lower because of the effect of snow over the surface that reduces the scattering coefficient.

4. Final Discussion

A serendipitous GNSS-R experiment performed with the SMAP radar receiver has provided a rather unique data set. The use of the Polarimetric Ratio (PR) at H-Pol and V-Pol from a GNSS-R spaceborne mission has been evaluated for the first time. This work provides an advance in the understanding of GNSS-R scatterometry over land surfaces and cryosphere enabled by the high gain of the radar antenna (~ 36 dB) and the use of two orthogonal polarizations. Additionally, the second added value of this work is the analysis of waveform spreading due to the scattering process over the Earth's surface, showing the ability to detect different levels of AGB over Amazonian and Boreal forests, differentiating from deserts and the cryosphere. Values of soil moisture as provided by the SMAP's radiometer, and SWI and NDVI maps have been used here to help in the interpretation of the GNSS-R observables. It is found that despite the good correlation between PR and the soil moisture

values, the GNSS-R signatures simultaneously contain information about AGB, soil moisture, and topography, making it difficult to separate the contributions. These issues need to be addressed to potentially provide accurate soil moisture measurements (key-factor for studies of the water cycle that is a continuous sequence involving water in the atmosphere, on the continents, and in the ocean), and biomass measurements (key-factor for evaluation of the carbon cycle).

5. Conclusions and Future Opportunities

A GNSS-R experiment has been performed from the NASA's SMAP satellite after tuning the radar receiver to the GPS L2 frequency (1227.6 MHz). Delay Doppler Maps (DDMs) were computed on-ground using a clean-replica of the open-access L2C code. Upon investigation, it was determined that the optimum coherent integration time for this experiment was $T_{\text{coh}} = 5$ ms. The high gain of the SMAP's antenna allowed it to receive strong signals from a variety of scenes. First results have been presented to investigate the characteristics of the reflected waveforms over land surfaces and cryosphere. The main observations from this study are: (a) the Polarimetric Ratio (PR) provided by this data set and the soil moisture content provided by the SMAP's radiometer show a Pearson linear correlation factor $r \sim -0.6$; (b) the Signal-to-Noise at H-Pol (SNR_{H}) shows different mean levels for different terrain types: $\text{SNR}_{\text{H,Lakes}} \sim 25$ dB, $\text{SNR}_{\text{H,Sahara}} \sim 18$ dB, $\text{SNR}_{\text{H,Greenland}} = 17$ dB, $\text{SNR}_{\text{H,Boreal Forests}} \sim 13$ dB, $\text{SNR}_{\text{H,Tropical Forests}} \sim 12$ dB; (c) the waveforms' parameters show sensitivity to seasonal fluctuations over regions with seasonal changes of geophysical parameters expressed by NDVI, and SWI; (d) the spreading of the waveforms' leading and trailing edge reduces for higher values of AGB (from $\text{AGB}_{\text{Boreal}} \sim 100$ ton/ha to $\text{AGB}_{\text{Tropical}} \sim 350$ ton/ha); (e) the AGB shows a more pronounced effect in GNSS-R signatures (PR, SNR, leading & trailing edges width) than NDVI; (f) the GNSS signals are depolarized upon scattering over areas with rough topography or high levels of AGB; and (g) the large spreading of the waveforms over the Greenland's ice cap suggests that the GNSS signals penetrate the subsurface significantly, which opens the possibility of cryosphere monitoring using GNSS-R sensors from space.

While the GNSS-R experiment on SMAP was helpful in providing high SNR polarimetric data, the sampling characteristics are not optimal for process studies. On the other hand, the unprecedented improved spatio-temporal sampling provided by the NASA's CyGNSS suggests the possibility to use its data to study soil moisture and vegetation water content variability in the tropical latitudinal bands. A careful assessment should be performed of the potential synergies between CyGNSS and SMAP GNSS-R data sets to evaluate how the SMAP's high SNR polarimetric data could help elucidate some of the scattering mechanisms not observable with the CyGNSS lower antenna gain.

Acknowledgments: This research was carried out at the Jet Propulsion Laboratory (JPL), California Institute of Technology (Caltech), under a contract with the National Aeronautics and Space Administration (NASA). The JPL Research and Technology Development (R&TD) program is gratefully acknowledged. The authors would like to thank to Attila Komjathy and Anthony Mannucci from JPL for their useful help and support. The authors would like to thank Piles, M. for doing available SMAP radiometer data. The authors would like to thank the anonymous reviewers for their comments and suggestions. © 2017 California Institute of Technology. Government sponsorship acknowledged.

Author Contributions: All authors contributed significantly to this manuscript. Hugo Carreno-Luengo processed and analyzed the data; Stephen Lowe designed the experiment; Cinzia Zuffada provided advice and support; Stephan Esterhuizen and Shadi Oveisgharan worked on signal processing during the experiment.

Conflicts of Interest: The authors declare no conflict of interest.

References

1. Hall, C.D.; Cordey, R.A. Multistatic scatterometry. In Proceedings of the 1988 IEEE International Geoscience and Remote Sensing Symposium, Edinburgh, UK, 13–16 September 1988; pp. 561–652.
2. Martín-Neira, M. A Passive Reflectometry and Interferometry System (PARIS): Application to ocean altimetry. *ESA J.* **1993**, *17*, 331–355.

3. Martin-Neira, M.; D'Addio, S.; Buck, C.; Floury, N.; Prieto-Cerdeira, R. The PARIS ocean altimeter in-orbit demonstrator. *IEEE Trans. Geosci. Remote Sens.* **2011**, *49*, 2209–2237. [[CrossRef](#)]
4. Roussel, N.; Frappart, F.; Ramillien, G.; Darrozes, J.; Baup, F.; Lestarquit, L.; Ha, M.C. Detection of soil moisture variations using GPS and GLONASS SNR data for elevation angles ranging from 2° to 70°. *IEEE J. Sel. Top. Appl. Earth Obs. Remote Sens.* **2016**, *9*, 4781–4794. [[CrossRef](#)]
5. Cardellach, E.; Rius, A.; Martin-Neira, M.; Fabra, F.; Nogues-Correig, O.; Ribo, S.; Kainulainen, J.; Camps, A.; D'Addio, S. Consolidation the precision of interferometric GNSS-R ocean altimetry using airborne experimental data. *IEEE Trans. Geosci. Remote Sens.* **2014**, *52*, 2209–2237. [[CrossRef](#)]
6. Semmling, A.M.; Wickert, J.; Schön, S.; Stosius, R.; Gerber, T.; Markgraf, M.; Ge, M.; Beyerle, G. A zeppelin experiment to study airborne altimetry using specular Global Navigation Satellite System reflections. *Radio Sci.* **2013**, *48*, 427–440. [[CrossRef](#)]
7. Lowe, S.T.; LaBrecque, J.L.; Zuffada, C.; Romans, L.J.; Young, L.E.; Hajj, G.A. First spaceborne observation of an Earth-reflected GPS signal. *Radio Sci.* **2002**. [[CrossRef](#)]
8. Gleason, S.; Hodgart, S.; Sun, Y.; Gommenginger, C.; Mackin, S.; Adjrard, M.; Unwin, M. Detection and processing of bistatically reflected GPS signals from low Earth orbit for the purpose of ocean remote sensing. *IEEE Trans. Geosci. Remote Sens.* **2005**, *43*, 1229–1241. [[CrossRef](#)]
9. Unwin, M. TechDemoSat-1 and the GNSS reflectometry experiment. In Proceedings of the TechDemoSat-1 User Consultation Meeting, Southampton, UK, 5 March 2015.
10. Chew, C.; Shah, R.; Zuffada, C.; Hajj, G.; Masters, D.; Mannucci, A.J. Demonstrating soil moisture remote sensing with observations from the UK TechDemoSat-1 satellite mission. *Geophys. Res. Lett.* **2016**, *43*, 3317–3324. [[CrossRef](#)]
11. Camps, A.; Hyuk, H.; Pablos, M.; Foti, G.; Gommenginger, C.; Liu, P.W.; Judge, J. Sensitivity of GNSS-R spaceborne observations to soil moisture and vegetation. *IEEE J. Sel. Top. Appl. Earth Obs. Remote Sens.* **2016**, *9*, 4730–4732. [[CrossRef](#)]
12. Clarizia, M.P.; Ruf, C.; Cipollini, P.; Zuffada, C. First spaceborne observation of sea surface height using GPS-Reflectometry. *Geophys. Res. Lett.* **2016**, *42*, 5435–5441. [[CrossRef](#)]
13. Foti, G.; Gommenginger, C.; Jales, P.; Unwin, M.; Shaw, A.; Robertson, C.; Rosello, J. Spaceborne GNSS Reflectometry for ocean winds: First Results from the UK TechDemoSat-1 Mission. *Geophys. Res. Lett.* **2015**, *43*, 767–774. [[CrossRef](#)]
14. Tye, J.; Jales, P.; Unwin, M.; Underwood, C. The first application of stare processing to retrieve mean square slope using the SGR-ReSI GNSS-R experiment on TDS-1. *IEEE J. Sel. Top. Appl. Earth Obs. Remote Sens.* **2016**, *9*, 4669–4677. [[CrossRef](#)]
15. Yan, Q.; Huang, W. Spaceborne GNSS-R sea ice detection using Delay-Doppler Maps: First results from the UK TechDemoSat-1 mission. *IEEE J. Sel. Top. Appl. Earth Obs. Remote Sens.* **2016**, *9*, 4795–4801. [[CrossRef](#)]
16. Carreno-Luengo, H.; Camps, A.; Vila, P.; Munoz, J.F.; Cortiella, A.; Vidal, D.; Jane, J.; Catarino, N.; Hagenfeldt, M.; Palomo, P.; et al. ³Cat-2: An experimental nano-satellite for GNSS-R Earth observation: Mission concept and analysis. *IEEE J. Sel. Top. Appl. Earth Obs. Remote Sens.* **2016**, *9*, 4540–4551. [[CrossRef](#)]
17. Rose, R.; Wells, W.; Rose, D.; Ruf, C.; Ridley, A.; Nave, K. Nanosat technology and managed risk: An update of the CyGNSS microsatellite constellation mission development. In Proceedings of the 28th AIAA/USU Conference on Small Satellites, Logan, UT, USA, 2–7 August 2014; pp. 1–12.
18. Zavorotny, V.U.; Voronovich, A.G. Bistatic GPS signal reflections at various polarizations from rough land surface with moisture content. In Proceedings of the 2000 IEEE International Geoscience and Remote Sensing Symposium, Honolulu, HI, USA, 24–28 July 2000; pp. 2852–2854.
19. Larson, K.M.; Braun, J.J.; Small, E.E.; Zavorotny, V.U.; Gutmann, E.D.; Bilich, A.L. GPS multipath and its relation to near-surface soil moisture content. *IEEE J. Sel. Top. Appl. Earth Obs. Remote Sens.* **2010**, *1*, 91–99. [[CrossRef](#)]
20. SongHua, Y.; ZhaoNengCheng, F.; GongSoil, C. Moisture estimation based on BeiDou B1 interference signal analysis. *Sci. China Earth Sci.* **2016**, *12*, 2427–2440.
21. Motte, E.; Zribi, M.; Fanise, P.; Egido, A.; Darrozes, J.; Al-Yaari, A.; Baghdadi, N.; Baup, F.; Dayau, S.; Fieuzal, R.; et al. GLORI: A GNSS-R dual polarization airborne instrument for land surface monitoring. *Sensors* **2016**, *16*, 732. [[CrossRef](#)] [[PubMed](#)]

22. Jia, Y.; Savi, P. Polarimetric GNSS-R measurements for soil moisture and vegetation sensing. In Proceedings of the 2016 IEEE International Geoscience and Remote Sensing Symposium, Beijing, China, 10–15 July 2016; pp. 5260–5263.
23. Park, J.; Johnson, J.T.; Ouellete, J. Modeling polarimetric sea surface specular scattering for GNSS-R applications. In Proceedings of the 2016 IEEE International Geoscience and Remote Sensing Symposium, Beijing, China, 10–15 July 2016; pp. 1903–1904.
24. Camps, A.; Marchan-Hernandez, J.F.; Bosch-Lluis, X.; Rodriguez-Alvarez, N.; Ramos-Perez, O.; Valencia, E.; Tarongi, J.M.; Park, H.; Carreno-Luengo, H.; Alonso-Arroyo, A.; et al. Review of GNSS-R instruments and tools developed at the Universitat Politecnica de Catalunya-BarcelonaTech. In Proceedings of the 2014 IEEE International Geoscience and Remote Sensing Symposium, Quebec, QC, Canada, 13–18 July 2014; pp. 3826–3829.
25. Ferrazzoli, P.; Guerriero, L.; Pierdicca, N.; Rahmoune, R. Forest biomass monitoring with GNSS-R: Theoretical simulations. *Adv. Space Res.* **2011**, *47*, 1823–1832. [[CrossRef](#)]
26. Wu, X.R.; Jin, S.G. GPS-Reflectometry: Forest canopies polarization scattering properties and modelling. *Adv. Space Res.* **2014**, *54*, 863–870. [[CrossRef](#)]
27. Egido, A.; Paloscia, S.; Motte, E.; Guerriero, L.; Pierdicca, N.; Caparrini, M.; Santi, E.; Fontanelli, G.; Floury, N. Airborne GNSS-R soil moisture and above ground biomass observations. *IEEE J. Sel. Top. Appl. Earth Obs. Remote Sens.* **2014**, *7*, 1522–1532. [[CrossRef](#)]
28. Carreno-Luengo, H.; Amezaga, A.; Vidal, D.; Olive, R.; Munoz, J.F.; Camps, A. First Polarimetric GNSS-R Measurements from a Stratospheric Flight over Boreal Forests. *Remote Sens.* **2015**, *7*, 13120–13138. [[CrossRef](#)]
29. Entekhabi, D.; Njoku, E.; O'Neill, P.; Spencer, M.; Jackson, T.; Entin, L.; Im, E.; Kellogg, K. The Soil Moisture Active Passive Mission (SMAP). In Proceedings of the 2008 IEEE International Geoscience and Remote Sensing Symposium, Boston, MA, USA, 6–11 July 2008.
30. Carreno-Luengo, H.; Camps, A. Unified GNSS-R formulation including coherent and incoherent scattering components. In Proceedings of the 2016 IEEE International Geoscience and Remote Sensing Symposium, Beijing, China, 10–15 July 2016; pp. 4815–4818.
31. Gleason, S. Remote Sensing of Ocean, Ice and Land Surfaces Using Bistatically Scattered GNSS Signals From Low Earth Orbit. Ph.D. Thesis, University of Surrey, Surrey, UK, 2000.
32. Pei, Y. GNSS Reflectometry for Land Surface Monitoring and Buried Object Detection. Ph.D. Thesis, Poltecnico de Torino, Turin, Italy, 2014.
33. Ulaby, F.T.; Moore, R.K.; Fung, A.K. Radar remote sensing and surface scattering and emission theory. In *Microwave Remote Sensing: Active and Passive*; Addison-Wesley: Reading, MA, USA, 1982; Volume 2, p. 1008.
34. Piles, M.; Entekhabi, D.; Konings, A.G.; McColl, K.A.; Das, N.N.; Jagdhuber, T. Multi-temporal microwave retrievals of soil moisture and vegetation parameters from SMAP. In Proceedings of the 2016 IEEE International Geoscience and Remote Sensing Symposium, Beijing, China, 10–15 July 2016; pp. 242–245.
35. Konings, A.G.; Piles, M.; Rotzer, K.; McColl, K.A.; Chan, S.K.; Entekhabi, D. Vegetation optical depth and scattering albedo retrieval using time series of dual polarized L-band radiometer observations. *Remote Sens. Environ.* **2016**, *172*, 178–189. [[CrossRef](#)]
36. Pierdicca, N.; Guerriero, L.; Giusto, R.; Brogioni, M.; Egido, A. SAVERS: A simulator of GNSS reflections from bare and vegetated soils. *IEEE Trans. Geosci. Remote Sens.* **2014**, *52*, 6542–6554. [[CrossRef](#)]
37. Kandel, P.N. Estimation of above ground forest biomass and carbon stock by integrating LiDAR, satellite image and field measurement in Nepal. *Res. J. Agric. For. Sci.* **2014**, *2*, 1–6.
38. Soil Water Index [SWI]. Available online: <http://land.copernicus.eu/global/products/swi> (accessed on 10 February 2017).
39. Vegetation Index [NDVI]. Available online: <http://neo.sci.gsfc.nasa.gov/> (accessed on 7 February 2017).
40. Prigent, C.; Aires, F.; Jimenez, C.; Papa, F.; Roger, J. Multiangle backscattering observations of continental surfaces in ku-band (13 GHz) from satellites: Understanding the signals, particularly in arid regions. *IEEE Trans. Geosci. Remote Sens.* **2015**, *53*, 1364–1373. [[CrossRef](#)]
41. Liu, P.W.; Judge, J.; DeRoo, R.D.; England, A.W.; Bongiovanni, T.; Luke, A. Dominant backscattering mechanisms at L-band during dynamic soil moisture conditions for sandy soils. *Remote Sens. Environ.* **2016**, *178*, 104–112. [[CrossRef](#)]
42. McColl, K.A.; Entekhabi, D.; Piles, M. Uncertainty analysis of soil moisture and vegetation indices using aquarius scatterometer observations. *IEEE Trans. Geosci. Remote Sens.* **2014**, *52*, 4259–4272. [[CrossRef](#)]

43. Stephen, H.; Long, D.G. Modeling microwave emissions of the erg surfaces in the Sahara desert. *IEEE Trans. Geosci. Remote Sens.* **2005**, *43*, 2822–2830. [[CrossRef](#)]
44. Fabra, F. GNSS-R as a Source of Opportunity for Remote Sensing of the Cryosphere. Ph.D. Thesis, Universitat Politècnica de Catalunya, Barcelona, Spain, 2014.
45. Fabra, F.; Cardellach, E.; Nogues-Correig, O.; Oliveras, S.; Ribo, S.; Arco, J.C.; Rius, A.; Belmonte-Rivas, M.; Semmling, M.; Macelloni, G.; et al. GNSS-R for Studies of the Cryosphere. Workshop on GNSS-Reflectometry. Barcelona, Spain, 22 October 2010. Available online: <http://congress.cimne.com/gnss-r10/frontal/presentaciones/130.pdf> (accessed on 3 December 2016).
46. Boniface, K.; Braun, J.J.; McCreight1, J.L.; Nievinski, F.G. Comparison of snow data assimilation system with GPS reflectometry snow depth in the Western United States. *Hydrol. Process.* **2015**, *29*, 2425–2437. [[CrossRef](#)]
47. Maetzler, C. Applications of SMOS over terrestrial ice and snow. In Proceedings of the 3rd SMOS Workshop, DLR, Oberpfaffenhofen, Germany, 10–12 December 2001.
48. Belmonte Rivas, M.; Maslanik, J.A.; Axelrad, P. Bistatic scattering of GPS signals off arctic sea ice. *IEEE Trans. Geosci. Remote Sens.* **2010**, *48*, 1548–1553. [[CrossRef](#)]
49. MacGregor, J.A.; Fahnestock, M.A.; Catania, G.A.; Aschwanden, A.; Clow, G.D.; Colgan, W.T.; Gogineni, S.P.; Morlighem, M.; Nowicki, S.M.; Paden, J.D.; et al. A synthesis of the basal thermal state of the Greenland Ice Sheet. *AGU J. Geophys. Res. Earth Surf.* **2016**, *121*, 1328–1350. [[CrossRef](#)] [[PubMed](#)]
50. Wiehl, M. Potential of reflected GNSS signals for ice sheet remote sensing. *Prog. Electromagn. Res.* **2003**, *40*, 177–205. [[CrossRef](#)]



© 2017 by the authors. Licensee MDPI, Basel, Switzerland. This article is an open access article distributed under the terms and conditions of the Creative Commons Attribution (CC BY) license (<http://creativecommons.org/licenses/by/4.0/>).